An iterative Bayesian approach for liver analysis: tumors validation study

Release 0.00

Y. Taieb[1*], O. Eliassaf[1*], M. Freiman[1], L. Joskowicz[1], J. Sosna[2]

July 4, 2008

[1]School of Eng. and Computer Science, The Hebrew Univ. of Jerusalem, Israel.
[2]Dept. of Radiology, School of Medicine, Hadassah Hebrew Univ. Medical Center, Jerusalem, Israel.
Project homepage: http://www.cs.huji.ac.il/~freiman/LiverSeg
Email: freiman@cs.huji.ac.il
[*] Equal contribution

Abstract

We present a new method for the simultaneous, nearly automatic segmentation of liver contours, vessels, and tumors from abdominal CTA scans. The method repeatedly applies multi-resolution, multi-class smoothed Bayesian classification followed by morphological adjustment and active contours refinement. It uses multi-class and voxel neighborhood information to compute an accurate intensity distribution function for each class. Only one user-defined voxel seed for the liver and additional seeds according to the number of tumors inside the liver are required for initialization. The algorithm do not require manual adjustment of internal parameters. In this work, a retrospective study on a validated clinical dataset totaling 20 tumors from 9 patients CTAs' was performed. An aggregated competition score of 61 was obtained on the test set of this database. In addition we measured the robustness of our algorithm to different seeds initializations. These results suggest that our method is clinically applicable, accurate, efficient, and robust to seed selection compared to manually generated ground truth segmentation and to other semi-automatic segmentation methods.

Contents

1 Introduction

Liver tumors segmentation is a key task in many clinical applications. Clinical applications include hepatomegaly and liver cirrhosis assessment, hepatic volumetry, hepatic transplantation planning, liver regeneration after hepatectomy, evaluation and planning for resection liver surgery, and monitoring of liver metastases, among many others. However, most of these applications require the entire liver segmentation, including liver contour and volume estimation, blood vessels identification, and, when present, tumor detection and characterization. To be of practical clinical use, the segmentation must be accurate, robust, fast, and nearly automatic, so that the radiologist can perform it routinely without the assistance of a technician.

Nearly automatic CT-based liver segmentation is known to be a very challenging task. The main difficulties include the ambiguity of the liver boundary, the complexity of the liver surface, the presence of surrounding organs, the contrast variability between liver parenchyma and vessels, the different tumor sizes and shapes, and the presence of many small metastases.

Over the past decade, researchers have developed a variety of methods for semi-automatic and automatic segmentation and visualization of liver structures. Most of these methods segment only one structure (liver contours [1, 2, 3, 4, 5, 6, 7] or vessels [8]), or segment one structure at a time, usually starting with the liver surface, followed by the vessels and the tumors. The individual structure segmentation uses various techniques, such as intensity thresholding, region growing, and level-sets based methods. For example, [9, 10] use adaptive binary thresholding to separately segment the liver surface, vessels, and tumors, followed by a deformable model refinement for each. Since it does not use voxel neighborhood information, it may yield noisy or erroneous liver surface segmentations, especially when large tumors are present, as they bias the intensity distribution function. Peitgen et al. [11] describe an edge-based segmentation method for the liver contour and an interactive region-growing method for the vessels and tumors. Since it requires many seeds per CT slice, it is of limited clinical use.

A key observation is that by considering each liver structure individually, the intrinsic relations between the liver parenchyma, vessels, and tumors are lost. This makes the classification more sensitive and error-prone. As an alternative, we presented a new method for the simultaneous segmentation of liver contours, vessels, and metastatic lesions from abdominal CTA scans [12]. The method repeatedly applies multi-resolution, multi-class smoothed Bayesian classification followed by morphological adjustment and active contours refinement. The method requires only one or two seeds (in case of presence of large tumors) for initialization, with no manual adjustment of internal parameters. By using the multi-class and voxel neighborhood information, it significantly improves the discrimination quality of the intensity distribution function for each class. The multi-resolution iterative approach allows the segmentation of the entire liver surface without prior shape information and/or significant user interaction. Our method yields accurate and robust results on two clinically validated datasets totaling 56 CTA studies, and achieved a very high score compared to other semi-automatic methods presented in the MICCAI 2007 grand-challenge for liver segmentation [13]. In this work we described the tumors segmentation validation study of our method on the current MICCAI 2008 grand-challenge workshop [14] database.

2 Method

Our method consists of four steps: 1) multi-class intensity model generation; 2) voxel classification; 3) morphological adjustment, and; 4) geodesic active contours refinement. The steps are performed in sequence and repeatedly applied to the image until no further changes occur. After each iteration, the internal parameters of the multi-class intensity model are updated. This repetitive updating is designed to overcome a

biased classification due to ambiguous liver boundaries and biased seed selection. The classification updates the classes intensity models by first computing the mean and variance of the liver and tumor classes from the current liver and tumor regions, and then updates the background classes by computing their mean and variance parameters. The output of the classification process is a labels map, which classify each voxel as either background, liver, blood vessels, or tumors. The morphological adjustment and the active contours refinement are then applied on the resulting regions to find the refined liver and tumors regions. The iterations are necessary for two reasons. The first is to fine-tune the intensity model which improve the classification and the second is to minimize the influence of the initial voxel seed selection.

To speed up the segmentation and make it more robust and accurate, we use a multi-resolution approach. The first few iterations are performed on a downsampled CTA dataset to obtain a rough contour segmentation. Subsequent iterations are performed on the original CTA dataset until no further improvements can be made. To improve the accuracy of tumors segmentation, a refinement iteration is applied to each tumor Region Of Interest (ROI) separately. We describe each step in detail next.

2.1 Multi-class intensity model generation

The first step is the construction of an intensity model that differentiates between the liver parenchyma, the liver inner vessels, the tumors, and the remaining organs and tissues, which are interpreted as background. The main challenges are the ambiguous boundary between the liver parenchyma and the outside organs (e.g the kidney), the ambiguous boundary between liver parenchyma and the liver vessels, and the similarity between lesions intensity values and other background values.

To overcome these difficulties, we first classify the voxels into two main classes, liver and lesions, according to their graylevel value. A refined five-class model is then built for each main class. The central class is the main class (e.g. liver or tumor); the remaining four classes represent other organs and tissues. We model each class with a normal distribution defined by its mean intensity value and variance. In the initial model, the mean and the variance of a rectangular neighborhood around one manually selected seed inside the liver and additional seeds inside the liver tumors (one seed for each tumor is required, Fig. 1(a,d)) are computed and interpreted as the parameters of the liver and tumor classes. In subsequent iterations, the segmented region from the previous iteration is used to compute the mean and the variance of the liver and tumor classes. The remaining four classes model background organs with intensities above/below the liver and tumor values.

Formally, the liver and tumor classes are defined as: X_{liver},X_{tumor} where

$$X_{central} \sim N(\mu_{central}, \sigma^2_{central}) \tag{1}$$

where $central \in \{liver, tumor\}$. For each object class ($liver, tumor$) we defined other four background classes:

$$X_i \sim N(\mu_i, \sigma_i^2) \tag{2}$$

for each i, $i \in \{near\_low, near\_high, far\_low, far\_high\}$, where $central$ is the liver or tumor class. The means of these classes defined as:

$$\begin{aligned} \mu_{near\_high} &= \mu_{central} + k_{near} \times \sigma_{central} \\ \mu_{near\_low} &= \mu_{central} - k_{near} \times \sigma_{central} \\ \mu_{far\_high} &= \mu_{central} + k_{far} \times \sigma_{central} \\ \mu_{far\_low} &= \mu_{central} - k_{far} \times \sigma_{central} \end{aligned} \tag{3}$$

The 'far' classes represent voxels with a very high probability to belong to the background, while the 'near' classes represent voxels in the ambiguous boundary of the objects. The factors k_{near} and k_{far} are determined from Chebyshev's inequality:

$$Pr(|X_i - \mu_{central}|) \geq k\sigma_{central}) \leq \frac{1}{k^2} \tag{4}$$

This inequality ensures that at least $(1-\frac{1}{k^2}) \times 100\%$ of the values are within k standard deviations from the mean. By setting $k_{near} = 2.2$ and $k_{far} = 4$, we ensure that at least 80% of the main class voxels will be classified as belonging to the main class, and at least 70% of the voxels that belong to the *near* classes will be classified as *near*, even if the normal distribution assumption is incorrect. This ensures that each voxel from the ambiguous class boundary has a high probability of being in either the *central* and *near* classes. Its final classification is then determined from its relation to neighboring voxels. Initially, we set $\sigma_i = \sigma_{central}$ for all classes.

2.2 Voxel classification

This step uniquely classifies each voxel according to its intensity value and its neighboring voxels [15]. Neighborhood information is important since voxel intensity values are correlated. First, we use Bayes rule to compute the probability $C_{(j,i)}$ of a voxel V_j with intensity value v_j to belong to class c_i, where $i \in \{central, near\_low, near\_high, far\_low, far\_high\}$:

$$Pr(c_i|v_j) \propto Pr(v_j|c_i)Pr(c_i) \tag{5}$$

where $Pr(c_i|v_j)$ is obtained from the intensity model (Sec. 2.1). Since $Pr(c_i)$ is usually unavailable, we use a uniform distribution. The resulting five maps quantify the membership probability of each voxel to each class.

Next, we incorporate the neighborhood information to the classification process by smoothing the probability maps $C_{(j,i)}$ for each class i separately using an anisotropic diffusion filter [16]. The anisotropic smoothing process smoothes small islands in the membership probability maps considered as mis-classifications while preserving sharp edges between different objects.

Finally, we apply the Maximum Posterior (MAP) rule:

$$C_{(j,final)} = \underset{c_i}{\operatorname{argmax}}\, Pr(c_i|v_j) \tag{6}$$

to set the final membership of each voxel to the class with the highest probability that the voxel belongs to it. The binary segmentation image is generated by selecting only the voxels that belong to the central class.

This step is applied twice, once for the liver class, and again for the tumor class. During the tumors classification, the liver class is considered as part of the background classes. The results are combined by taking into account only the tumor voxels inside the liver. Since the vessels appear as bright regions inside the liver, the vessels class is defined by the the X_{near_high} class for voxels inside the liver.

2.3 Adaptive morphological adjustment

The third step is the identification of the liver and tumors regions. The previous classification yields most of the liver region, with additional disconnected regions outside the liver, and holes inside the liver. The regions outside the liver correspond to anatomical structures with intensity values similar to the liver, such as the kidney and the spleen. The holes correspond to small tumors and artery and portal veins inside the

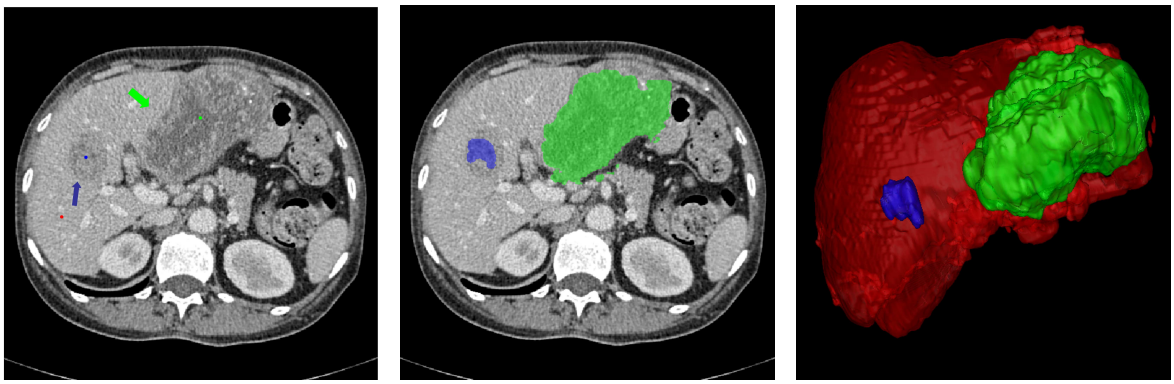

(a) IMG07 - Original slice (b) segmentation result (c) 3D view

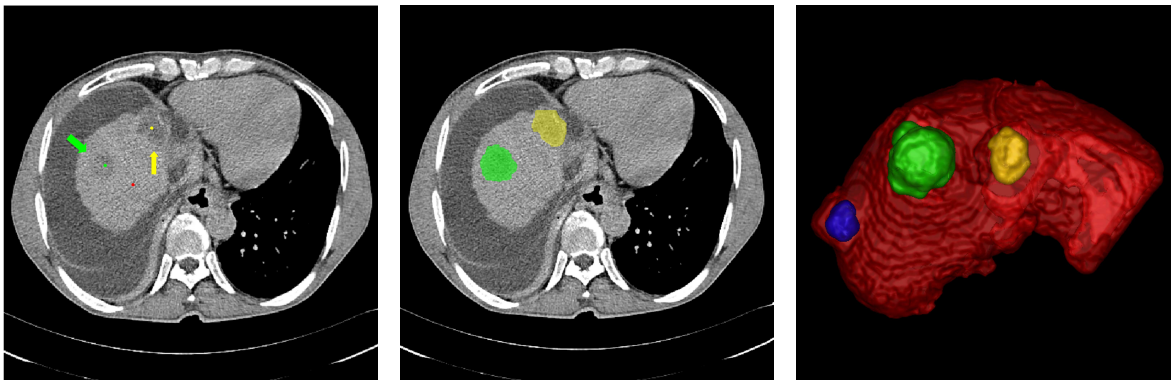

(d) IMG05 - Original slice (e) segmentation result (f) 3D view

Figure 1: Example of segmented livers and tumors. (a)-(c) Best case result (IMG07). (d)-(f) worst case result (IMG05). The coloured dots in images (a) and (d), illustrate the initialization seeds required as input by our method. The arrows indicate tumors locations. The images in this figure produced using itksnap [17].

liver whose intensity values are distinctly different from the liver intensity values because of the imaging contrast agent. To obtain the correct liver segmentation, the disconnected regions must be eliminated, and the holes inside the liver must be filled. This is done with adaptive morphological operations.

We first remove the disconnected regions outside the liver by identifying the largest connected component in the labeled image. Next, the holes inside the liver are classified as tumor or vessels according to the intensity model in Sec. 2.1. Finally, we adjust the liver and tumors boundaries with an adaptive morphological opening operator. To overcome the inter-patient variablity of the liver and tumors sizes, the radiuses of the morphological operators linearly depend on the estimated liver and tumors volumes.

2.4 Active contours refinement

The classification and the morphological adjustment may miss parts of the liver and tumors volumes. In addition, the objects boundaries may be inaccurate in several regions. To correct this, we repeatedly apply a fine-tuning active contours segmentation [18]. The active contours segmentation drives the initial surface according to a feature map generated from the original image. To provide a good feature image to the active

Table 1: Results of the comparison metrics and scores for all ten test cases. The first column indicates the dataset.

Dataset	Overlap Error		Volume Diff.		Avg. Dist.		RMS Dist.		Max. Dist.		Total
	[%]	Score	[%]	Score	[mm]	Score	[mm]	Score	[mm]	Score	Score
IMG05 L1	27.68	79	22.94	76	2.17	45	2.68	63	8.62	78	68
IMG05 L2	55.80	57	124.49	0	3.37	15	4.74	34	15.77	61	33
IMG05 L3	48.19	63	89.48	7	2.70	32	3.34	53	9.26	77	46
IMG06 L1	71.12	45	70.99	26	2.54	36	3.26	55	7.95	80	48
IMG06 L2	36.33	72	21.79	77	0.93	77	1.27	82	4.84	88	79
IMG07 L1	21.06	84	9.03	91	2.42	39	3.49	51	15.64	61	65
IMG07 L2	26.14	80	6.76	93	1.19	70	1.58	78	6.92	83	81
IMG08 L1	15.49	88	12.53	87	1.76	56	2.62	63	13.82	65	72
IMG09 L1	41.40	68	34.64	64	1.48	63	2.17	70	7.52	81	69
IMG10 L1	51.61	60	50.97	47	3.35	15	3.81	47	9.07	77	49
Average	39.48	70	44.36	57	2.19	45	2.90	60	9.94	75	61

contours module, we generate a new image with a windowing function:

$$I^{'}(x) = \begin{cases} \mu_{liver} + \sigma_{liver} & \text{if } I(x) > \mu_{liver} + \sigma_{liver}, \\ I(x) & \text{if } \mu_{liver} - \sigma_{liver} \leq I(x) \leq \mu_{liver} + \sigma_{liver}, \\ \mu_{liver} - \sigma_{liver} & \text{if } I(x) < \mu_{liver} - \sigma_{liver}. \end{cases} \quad (7)$$

where I is the original CTA data, I' is the new image, and μ_{liver} and σ_{liver} are the liver class parameters as computed in the intensity model. This process applied for both the liver and tumors boundaries.

3 Experimental results

We implemented our method using the ITK software library [19] and the smoothed Bayesian classification module [20]. Computations were performed on an Intel Core2 Quad 2.4 GHz PC with 3GB of memory.

We performed a retrospective study on the database provided by the MICCAI 2008 3D Liver Tumors Segmentation workshop [14]. The dataset consists of 20 tumors from clinical datasets of 9 patients. It is divided into two groups. The first group consists of 10 tumors from 4 patients and is used for training and fine-tuning of the algorithm; The second group consists of 10 tumors form 5 patients and is used to evaluate segmentation algorithms. Evaluation followed the method described in [13]. We compared our segmentation results to the ground-truth using five metrics: 1) volumetric overlap; 2) relative absolute volume difference; 3) average symmetric absolute surface distance; 4) symmetric RMS surface distance, and; 5) maximum symmetric absolute surface distance. Table 1 summarizes the results. Based on these metrics results an aggregate score was computed. Our average score was 61. The mean (std) computation time for each liver, including segmentation of the entire liver, blood vessels and tumors was 8.34 (2.47) minutes . Note that the required user-time was only a few seconds for seeds selection. Fig. 1 illustrates our results on the test set for the best and worst cases.

In addition, we measured the robustness of our method to three different seeds initializations on the 10 training tumors. Table 2 summarizes the results. These results show that our method is very robust to different seeds initializations, whereas other semi-automatic methods, which require significantly more user interaction, are prone to be less robust.

Table 2: Results of the comparison between metrics and final scores for different initializations on the ten training cases. The values are the mean pairwise difference between the results of three initializations

Dataset	Overlap Error [%]	Volume Diff. [%]	Avg. Dist. [mm]	RMS Dist. [mm]	Max. Dist. [mm]	Total Score
IMG01 L1	1.05	0.21	0.24	0.28	1.05	0
IMG01 L2	0.34	0.01	0.01	0.04	0.22	0
IMG02 L1	8.52	0.27	0.29	0.13	6.23	2
IMG02 L2	0.04	0.01	0.02	0.1	0.01	0
IMG02 L3	0.76	0.05	0.05	0.02	0.82	0.67
IMG03 L1	14.17	0	0.09	1.18	0.29	0.67
IMG04 L1	1.32	0.18	0.32	2.97	1.94	6
IMG04 L2	2.94	0.06	0.08	0	0.96	4
IMG04 L3	0.71	0.02	0.03	0.27	0.25	1.33
IMG04 L4	0.35	0.2	0.5	0.97	0.63	2.67
Average	3.02	0.1	0.16	0.6	1.24	1.73

4 Conclusion

We have presented a new nearly-automatic segmentation method for liver analysis. The main advantage of our method is that it simultaneously segments the liver contour, the blood vessels, and tumors inside the liver with only several user-selected seeds. Experimental results on the current MICCAI 2008 grand-challenge workshop database [14], totaling 20 tumors from 9 patients, show that our method is clinically applicable, accurate, efficient, and robust to seed selection whencompared to manually generated ground truth segmentation. In the future, we plan develop an integrated software package for the visualization and quantitative analysis of the liver to support diagnosis and surgical planning.

References

[1] T. Okada, R. Shimada, Y. Sato, M. Hori, K. Yokota, M. Nakamoto, Y.W. Chen, H. Nakamura, and S. Tamura. Automated segmentation of the liver from 3D CT images using probabilistic atlas and multi-level statistical shape model. In *Proc. of the 10th Int. Conf. of Med. Image Comp. and Computed Aided Intervention (MICCAI'07)*, volume 4791 of *LNCS*, pages 86–93, 2007. 1

[2] T. Heimann, I. Wolf, and H.P. Meinzer. Active shape models for a fully automated 3D segmentation of the liver - an evaluation on clinical data. In *Proc. of the 9th Int. Conf. of Med. Image Comp. and Computed Aided Intervention (MICCAI'06)*, volume 4191 of *LNCS*, pages 41–48, 2006. 1

[3] R. Pohle and K. Toennies. Segmentation of medical images using adaptive region growing. In *SPIE Med. Imaging*, volume 4322, pages 1337–1346, 2001. 1

[4] A. Schenk, G.P.M. Prause, and H.O. Peitgen. Efficient semiautomatic segmentation of 3D objects in medical images. In *Proc. of the 3rd Int. Conf. of Med. Image Comp. and Computed Aided Intervention (MICCAI'00)*, volume 1935 of *LNCS*, pages 186–195, 2000. 1

[5] T. Chen and D. Metaxas. A hybrid framework for 3D medical image segmentation. *Med. Image Analysis*, 9(6):547–565, 2005. 1

[6] S. Pan and M. Dawant. Automatic 3d segmentation of the liver from abdominal CT images: A level-set approach. In *SPIE Medical Imaging*, volume 4322, pages 128–138, 2001. 1

[7] H. Lamecker, T. Lange, and M. Seebass. A statistical shape model for the liver. In *Proc.of the 5th Int. Conf. of Med. Image Comp. and Computed Aided Intervention (MICCAI'02)*, volume 2489 of *LNCS*, pages 421–427, 2002. 1

[8] C.I. Fetita, O. Lucidarme, F.J. Preteux, and P. Grenier. CT hepatic venography: 3D vascular segmentation for preoperative evaluation. In *Proc. of the 8th Int. Conf. of Med. Image Comp. and Computed Aided Intervention (MICCAI'05)*, volume 3750 of *LNCS*, pages 830–837, 2005. 1

[9] L. Gao, D.G. Heath, B.S. Kuszyk, and E.K. Fishman. Automatic liver segmentation technique for 3D visualization of CT data. *Radiology*, 201(2):359–364, 1996. 1

[10] L. Soler, H. Delingette, G. Malandain, J. Montagnat, N. Ayache, C. Koehl, O. Dourthe, B. Malassagne, M. Smith, D. Mutter, and J. Marescaux. Fully automatic anatomical, pathological, and functional segmentation from CT scans for hepatic surgery. *Computer Aided Surgery*, 6(3):131–142, 2001. 1

[11] H. Bourquain, A. Schenk, F. Link, B. Preim, G. Prause, and H.O. Peitgen. Hepavision2a software assistant for preoperative planning in living related liver transplantation and oncologic liver surgery. In *Proc. of the 16th Conf. on Comp. Assisted Radiology and Surgery (CARS'02)*, pages 341–346, 2002. 1

[12] M. Freiman, O. Eliassaf, Y. Taieb, L. Joskowicz, and J. Sosna. A bayesian approach for liver analysis: algorithm and validation study. In *Proc. of the 11th Int. Conf. of Med. Image Comp. and Computed Aided Intervention (MICCAI'08)*, 2008. (in press). 1

[13] B.V Ginneken, T. Heimann, and M. Styner. 3D segmentation in the clinic: A grand challenge. In T. Heimann, M. Styner, and B. van Ginneken, editors, *3D Segmentation in the Clinic: A Grand Challenge*, pages 7–15., 2007. http://www.sliver07.org. 1, 3

[14] http://lts08.bigr.nl/. 1, 3, 4

[15] P.C. Teo, G. Sapiro, and B.A. Wandell. Anisotropic smoothing of posterior probabilities. In *Proc. of the 1997 Int. Conf. on Image Processing (ICIP'97)*, pages 675–678, 1997. 2.2

[16] P. Perona and J. Malik. Scale-space and edge detection using anisotropic diffusion. *IEEE Trans. Patt. Anal. Mach. Intelligence*, 12(7):629–639, 1990. 2.2

[17] P.A. Yushkevich, J. Piven, C.H. Heather, R. Gimpel Smith, H. Sean, J.C. Gee, and G. Guido. User-guided 3D active contour segmentation of anatomical structures: Significantly improved efficiency and reliability. *Neuroimage*, 31(3):1116–1128, 2006. http://www.itksnap.org/. 1

[18] V. Caselles, R. Kimmel, and G. Sapiro. Geodesic active contours. *Int. J. Comp. Vision*, 22(1):61–97, 1997. 2.4

[19] L. Ibanez, W. Schroeder, L. Ng, and J. Cates. *The ITK Software Guide*. Kitware, Inc. ISBN 1-930934-15-7, http://www.itk.org/ItkSoftwareGuide.pdf, 2005. 3

[20] J. Melonakos, K. Krishnan, and A. Tannenbaum. An ITK filter for bayesian segmentation: itkbayesianclassifierimagefilter. Insight Journal, http://www.insight-journal.org, 2006. 3